

Unconventional charge-density wave in $\text{Sr}_3\text{Ir}_4\text{Sn}_{13}$ cubic superconductor revealed by optical spectroscopy study

A. F. Fang,¹ X. B. Wang,¹ P. Zheng,¹ and N. L. Wang^{1,2}¹*Beijing National Laboratory for Condensed Matter Physics, Institute of Physics, Chinese Academy of Sciences, Beijing 100190, People's Republic of China*²*Collaborative Innovation Center of Quantum Matter, Beijing, China*

(Received 17 December 2013; revised manuscript received 26 June 2014; published 14 July 2014)

$\text{Sr}_3\text{Ir}_4\text{Sn}_{13}$ is an interesting compound showing the coexistence of structural phase transition and superconductivity. The structural phase transition at 147 K leads to the formation of a superlattice. We perform optical spectroscopy measurements across the structural phase transition on single-crystal samples of $\text{Sr}_3\text{Ir}_4\text{Sn}_{13}$. The optical spectroscopy study reveals an unusual temperature-induced spectral weight transfer over a broad energy scale, yielding evidence for the presence of electron correlation effects. Below the structural phase transition temperature an energy gap-like suppression in optical conductivity was observed, leading to the removal of partial itinerant carriers near the Fermi level. Unexpectedly, the suppression appears at a much higher energy scale than expected for the usual charge-density-wave phase transition.

DOI: [10.1103/PhysRevB.90.035115](https://doi.org/10.1103/PhysRevB.90.035115)

PACS number(s): 78.20.-e, 71.45.Lr, 74.70.-b

Transition-metal compounds are well known for exhibiting rich and interesting physical properties such as charge- or spin-density wave [1–4], superconductivity [5,6], and modulated lattice distortion [7,8]. The interplay between two very different electronic phenomena is one of the fundamental interests in condensed-matter physics. For example, the layered transition metal dichalcogenides TX_2 (T, transition metal; X, chalcogen), ordinarily possessing charge-density wave (CDW) instability and its coexistence/competition with superconductivity, are central characteristics of this family [9–11]. Lately, the $5d$ transitional metal ditelluride $\text{Ir}_{1-x}\text{Pt}_x\text{Te}_2$ has attracted particular attention for the competing phenomenon between structural instability and superconductivity [7,12,13].

A very recent example is the cubic superconductor $\text{Sr}_3\text{Ir}_4\text{Sn}_{13}$ with $T_c = 5$ K [14–16]. This compound undergoes a structural phase transition at $T^* \simeq 147$ K, evolving from the I structure ($Pm\bar{3}n$) to an I' structure ($I\bar{4}3d$) accompanied by a doubling of the unit cell with decreasing temperature across the transition [16]. Concerning the structural phase transition, Klintberg *et al.* found that a superlattice distortion emerged below the structural phase transition and assigned it to a CDW modulation [16]. A muon spin rotation (μSR) study on the isovalent compound $\text{Ca}_3\text{Ir}_4\text{Sn}_{13}$ ($T_c = 7$ K, $T^* \simeq 33$ K) confirmed that the structural phase transition was a nonmagnetic transition [17], making the CDW scenario more plausible and excluding the possibility of the ferromagnetic spin-fluctuation scenario [18]. Despite the extensive studies on $(\text{Sr,Ca})_3\text{Ir}_4\text{Sn}_{13}$, the origin of the structural transition and its relation to superconductivity are yet to be clarified. On the other hand, it is well known that CDW often occurs in low-dimensional electronic systems, while such instability is not expected to develop in a three-dimensional (3D) system. $\text{Sr}_3\text{Ir}_4\text{Sn}_{13}$ supplies us a precious opportunity to investigate the interplay between possible CDW instability and superconductivity in a 3D cubic compound. It is also argued that the structural phase transition in $(\text{Sr,Ca})_3\text{Ir}_4\text{Sn}_{13}$ is a pressure-induced structural quantum critical point [16], which makes the compounds more interesting.

It is of great significance to understand the origin of the structural phase transition, since it is the essential step towards understanding the mechanism of superconductivity. In this work, we report an optical spectroscopy investigation on well-characterized $\text{Sr}_3\text{Ir}_4\text{Sn}_{13}$ single-crystal samples. We show that the structural phase transition is associated with the formation of a partial energy gap at the Fermi surface. A significant number of itinerant carriers are lost due to the opening of the gap. We suggest an unconventional CDW scenario to account for the second-order structural phase transition.

$\text{Sr}_3\text{Ir}_4\text{Sn}_{13}$ single crystals were synthesized by self-flux technique in a procedure similar to that in earlier reports [14,19]. The Sn flux was initially removed from single crystals using a centrifuge at approximately 575°C , and then the residual flux was etched in concentrated hydrochloric acid. Shiny 3D samples were successfully extracted with maximum dimensions of $3 \times 5 \times 5$ mm³. In order to keep the whole sample at the same temperature with the sample holder during optical spectroscopy measurements, we picked a single crystal with a large flat surface and polished its opposite plane until a thin sheet obtained. The flat surface was identified to be the (110) plane by single-crystal x-ray diffraction (XRD) measurements, as displayed in Fig. 1. The I phase structure with space group $Pm\bar{3}n$ and lattice parameter $a = 9.8156$ Å were obtained from single-crystal XRD data at room temperature.

The dc resistivity measurements were conducted on a commercial Quantum Design physical properties measurement system by a four-probe method. Specific heat data were obtained by a relaxation-time method using the system. The magnetic susceptibility was measured on a Quantum Design superconducting quantum interference device vibrating sample magnetometer system (SQUID-VSM). Figure 2(a) presents the temperature dependence of resistivity ρ for $\text{Sr}_3\text{Ir}_4\text{Sn}_{13}$ single crystals. A distinct anomaly is observed at $T^* = 147$ K on cooling, while no obvious hysteresis of T^* is found upon warming (not shown). The specific heat C_p also reveals a sharp anomaly at corresponding T^* , as shown in Fig. 2(b).

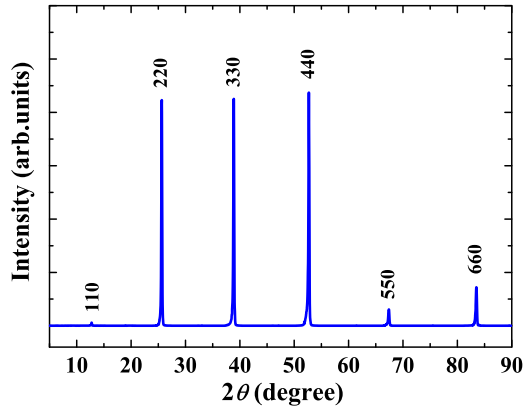


FIG. 1. (Color online) The χ -ray diffraction patterns of $\text{Sr}_3\text{Ir}_4\text{Sn}_{13}$ single crystals at room temperature.

The characteristic λ -like shape of the sharp anomaly identifies the T^* anomaly as a second-order phase transition. Figure 2(c) shows that the T^* phase transition leads to a sudden drop in magnetic susceptibility, which is similar to that of IrTe_2 [13]. As exhibited in Figs. 2(c)–2(e), the phase transition creates clear anomalies at the same T^* for magnetic susceptibility, resistivity, and specific heat.

As reported in the previous work, the structural phase transition at 147 K results in a 1.1×10^{-4} emu/mol change in Pauli susceptibility [16]. Our result is consistent with this. Another striking point is that the magnetic susceptibility remains negative even above the phase transition. As is well known, the closed electronic shells or fully occupied

bands would contribute to the diamagnetism, so-called Larmor diamagnetism. Since iridium is a $5d$ transition metal, additionally, and the crystals contain Sn_{12} cages in the crystal structure, Larmor diamagnetism is probably sufficient to exceed the paramagnetic Pauli spin susceptibility χ_P of the conduction carriers. Therefore, the magnetic susceptibilities of $\text{Sr}_3\text{Ir}_4\text{Sn}_{13}$ compounds are diamagnetic. Considering the result (obtained below) that about 30% of itinerant carriers at Fermi surfaces are lost and χ_P is proportional to the conduction carriers, the diamagnetism is further enhanced below the phase transition.

Another significant phenomenon revealed by the electrical resistivity $\rho(T)$ is a superconducting phase transition at $T_c = 5$ K. Figure 3(a) shows the temperature-dependent low-temperature magnetic susceptibility for $\text{Sr}_3\text{Ir}_4\text{Sn}_{13}$ single crystals in $H = 50$ Oe parallel to the (110) plane with zero-field-cooled and field-cooled processes. The low-temperature magnetic susceptibility suggests the Meissner effect of the superconductivity below 5 K. The obvious peak in specific heat at T_c shown in Fig. 3(b) confirms the bulk superconductivity for $\text{Sr}_3\text{Ir}_4\text{Sn}_{13}$ single crystals. It is known that the specific heat at low temperatures can be approximately written by $C_p/T = \gamma + \beta T^2 + \eta T^4$, with the three terms on the right-hand side representing the electron, phonon, and anharmonic phonon contributions, respectively. The linear fit of normal-state C/T as a function of T^2 [solid line in Fig. 3(b)] provides the electronic specific heat coefficient $\gamma = 40.0(1)$ mJ K $^{-2}$ mol $^{-1}$, giving a good agreement with previous measurements [15]. Since γ is proportional to $N(E_F^0)$ (the electronic density of states near the Fermi level), $N(E_F^0)$ should be rather large, indicating the presence of relatively narrow energy bands.

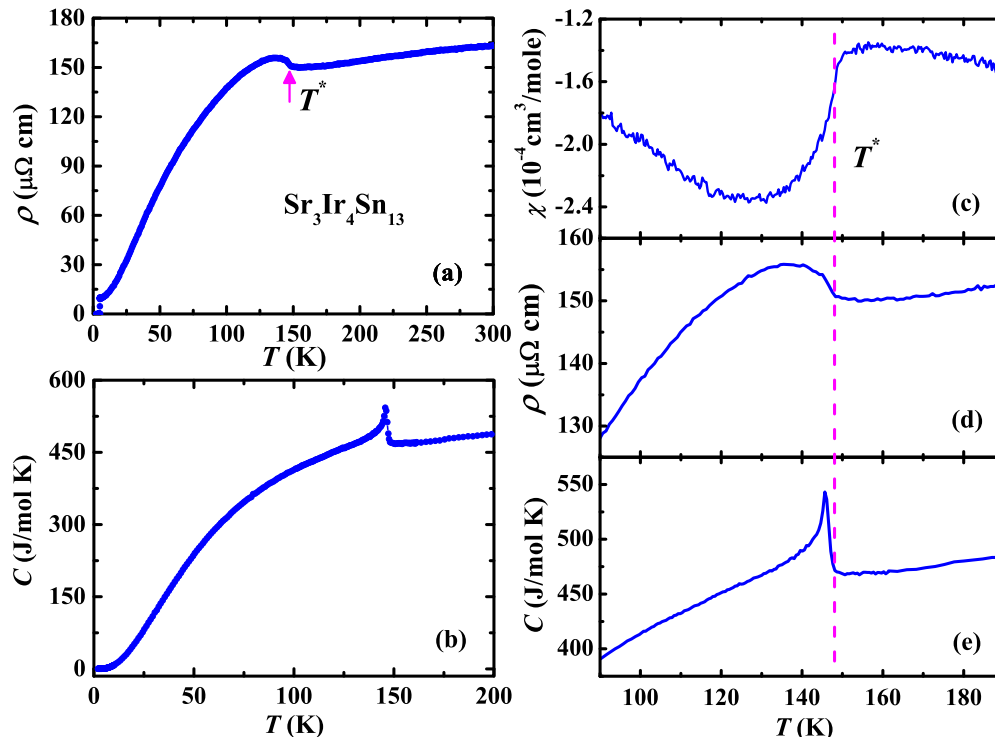


FIG. 2. (Color online) Physical properties of $\text{Sr}_3\text{Ir}_4\text{Sn}_{13}$ single crystals. (a) Resistivity ρ versus temperature in the range of 2 to 300 K. (b) Temperature dependence of specific heat C with zero applied field. (c–e) Temperature-dependent magnetic susceptibility (a), resistivity (b), and specific heat (c) from 90 to 190 K, respectively. The dashed line indicates the phase transition beginning at $T^* = 147$ K.

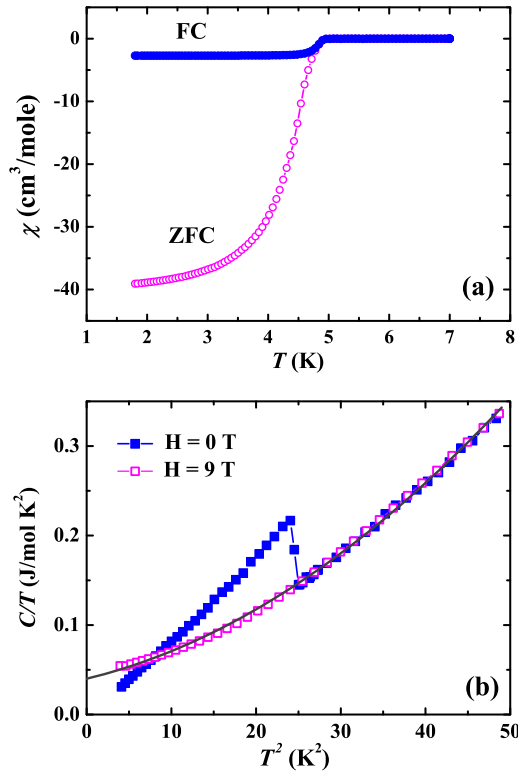


FIG. 3. (Color online) (a) Low-temperature magnetic susceptibility χ versus temperature for $\text{Sr}_3\text{Ir}_4\text{Sn}_{13}$ single crystals in $H = 50$ Oe parallel to the (110) plane with zero-field-cooled (ZFC) and field-cooled (FC) processes. (b) Specific heat of $\text{Sr}_3\text{Ir}_4\text{Sn}_{13}$ in the plot of C/T versus T^2 with 0 T and 9 T applied field perpendicular to the (110) plane; the solid line is the fitting result using the relation $C = \gamma T + \beta T^3 + \eta T^5$ after the superconductivity is completely suppressed by a magnetic field of 9 T.

Therefore, electron correlation effects might not be weak in $\text{Sr}_3\text{Ir}_4\text{Sn}_{13}$.

The temperature-dependent (110)-plane optical reflectance data were measured on Bruker 113v, Vertex 80v, and grating-type spectrometers on shiny flat surfaces of $\text{Sr}_3\text{Ir}_4\text{Sn}_{13}$ superconducting single crystals over a broad frequency range, from 40 to 50 000 cm^{-1} (cm^{-1} relates to $1/\lambda$ in this paper). We first obtained the reflectivity $R(\omega)$ by an *in situ* gold and aluminum overcoating technique, further getting the real part of the conductivity $\sigma_1(\omega)$ by the Kramers-Kronig transformation of $R(\omega)$. Figure 4 displays the reflectance and optical conductivity spectra for $\text{Sr}_3\text{Ir}_4\text{Sn}_{13}$ single crystals with systematically varying temperature from 10 to 300 K. All the $R(\omega)$ approach unity at zero frequency, both above and below the T^* phase transition. A good metallic feature is obviously revealed, corresponding to the dc electric resistivity. There is a compelling phenomenon in the $R(\omega)$ spectra below the T^* phase transition, i.e., a prominent suppression feature below 4000 cm^{-1} (marked by an arrow), especially that at 10 K. Clarifying the suppression feature is crucial for elaborating the evolution of the electronic structure across the transition.

The suppression feature is clearly reflected in the optical conductivity spectra as well, shown in Fig. 4 (b). Apparent

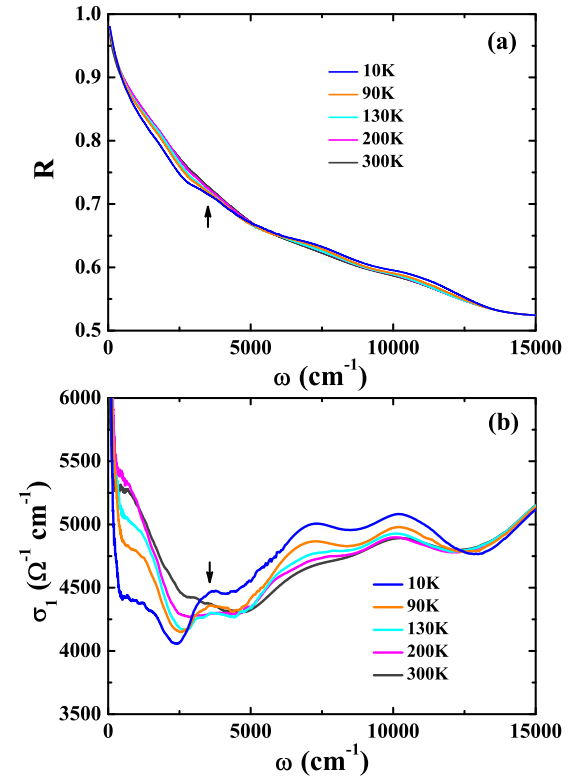


FIG. 4. (Color online) (a) The (110)-plane reflectance spectra of $\text{Sr}_3\text{Ir}_4\text{Sn}_{13}$ single crystals at various temperatures, with the black arrow marking the onset of the suppression feature. (b) Optical conductivity $\sigma_1(\omega)$ up to 15 000 cm^{-1} ; the black arrow points at the newly developed peaks.

Drude components can be observed at low frequencies in all spectral curves, indicating a good metallic response. Above the T^* phase transition, the low-frequency Drude component shows ordinary narrowing resulting from the reduced scattering with decreasing temperature, while an unconventional spectral weight transfer is observed from the low-energy midinfrared region to the high-energy interband transition region above 5000 cm^{-1} . Upon cooling the sample across the T^* phase transition, a significant spectral weight suppression develops in the Drude components and the suppressed spectral weight is transferred to the peak feature (marked by an arrow) forming at about 4000 cm^{-1} . Since the Drude component represents the contribution from conduction electrons, the suppression of the Drude components observed in our optical spectroscopy experiments suggests the removal of a part of the Fermi surface below the phase transition. At variance with other compounds possessing first-order structural phase transitions, e.g., IrTe_2 [13] or BaNi_2As_2 [20], where the optical conductivity spectra develop sudden and dramatic changes over broad frequencies across the phase transitions owing to the reconstruction of the band structures, the present case is more similar to some CDW materials such as 2H-TaS_2 [21], whose spectral suppression features are rather weak and evolve continuously with temperature. On the other hand, the unconventional spectral weight transfer also exists below the T^* phase transition. This unconventional spectral weight transfer may be ascribed to the correlation effect, e.g., the

intersite Coulomb repulsion, similar to some charge-ordering systems [22–24].

Aiming to further investigate the evolution of Drude components, the Drude-Lorentz model was applied to decompose the optical conductivity spectra into different components. The dielectric function can be written as [25]

$$\epsilon(\omega) = \epsilon_\infty - \sum_i \frac{\omega_{p,i}^2}{\omega_i^2 + i\omega/\tau_i} + \sum_j \frac{\Omega_j^2}{\omega_j^2 - \omega^2 - i\omega/\tau_j}, \quad (1)$$

where ϵ_∞ is the dielectric constant at high energy, and the middle and last terms are the Drude and Lorentz components, respectively. The Drude components describe the contribution from conduction electrons, while the Lorentz components represent the interband transitions. As indicated by the band structure calculations, for $\text{Sr}_3\text{Ir}_4\text{Sn}_{13}$, several different bands cross the Fermi level and the Fermi surfaces are rather complicated [16,26]. As a consequence, the conduction electrons are contributed by different bands and exhibit different behaviors. Therefore, we applied two Drude components analysis here. In order to reproduce the optical conductivity below $15\,000\text{ cm}^{-1}$ at 300 K, two Drude components, a narrow one and a broad one, and four Lorentz terms have to be used. The narrow one only occupies a small fraction of the spectral weight of the conduction electrons, while the broad Drude component takes up most of this spectral weight. However, an additional Lorentz component centered at 3500 cm^{-1} (L5 in Fig. 5) should be added at temperatures below the phase transition. Actually, such analysis has been widely applied to multiband systems, for example, Fe-based superconductors (although Fe-pnictide superconductors usually have five Fermi surfaces: three hole-type Fermi surfaces and two electron-type Fermi surfaces) [27–29].

Figure 5(a) illustrates the conductivity spectra at 10 and 300 K together with the Drude-Lorentz fitting components for $\text{Sr}_3\text{Ir}_4\text{Sn}_{13}$. It is found that the two Drude components narrow with decreasing temperature because of the metallic response, while the gapping of the Fermi surfaces mainly occurs in the broad Drude component. The results indicate that the gapping of the Fermi surfaces caused by the T^* phase transition mainly takes place on those Fermi surfaces where the electrons experience stronger scattering. Compared with the spectral weight distribution at 300 K, the spectral weight of D1 decreases and the suppression part of D1 is transferred to that of the added L5 as well as that of L2 and L3 at 10 K. Considering that two Drude components contribute to the conductivity, the formula $\omega_p = \sqrt{\omega_{p1}^2 + \omega_{p2}^2}$ could be used to obtain the overall plasma frequency ω_p , and then $\omega_p \approx 30\,530\text{ cm}^{-1}$ at 300 K and $\omega_p \approx 25\,750\text{ cm}^{-1}$ at 10 K are estimated. Therefore, the ratio of the square of the plasma frequency in the low temperature phase to that at 300 K is about 0.71, as shown in Fig. 5(b). It is well known that $\omega_p^2 = 4\pi ne^2/m^*$, where n is the carrier density and m^* is the effective mass. Provided that the effective mass of the itinerant carriers remains unchanged, the optical measurements reveal that roughly 29% of itinerant carriers are lost, obtained from the change in ω_p after the second-order phase transition, which agrees with the previous electronic structure calculations [16]. However, the overall scattering rate cannot be estimated by a simple summation of the two scattering rates of two

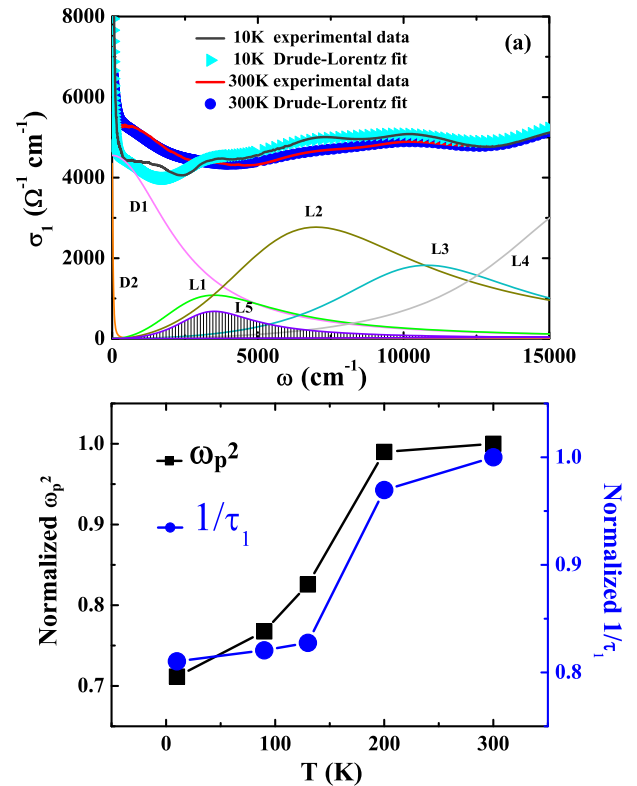


FIG. 5. (Color online) (a) Experimental $\sigma_1(\omega)$ data at 10 and 300 K up to $15\,000\text{ cm}^{-1}$. The Drude (D1, D2) and the Lorentz (L1–L5) terms acquired from a Drude-Lorentz fit for $T = 10\text{ K}$ below $15\,000\text{ cm}^{-1}$ are illustrated at the bottom. (b) Normalized total ω_p^2 (black line with squares) and $1/\tau_1$ (blue line with circles). Both parameters are normalized to the values of 300 K.

separate Drude components ($1/\tau = 1/\tau_1 + 1/\tau_2$); that only works out for one Drude component with multiple scattering channels. For two Drude component analysis the conductivity contributed by conduction electrons could be described by $\sigma_D = \frac{1}{4\pi} [\omega_{p1}^2/(\gamma_{D1} - i\omega) + \omega_{p2}^2/(\gamma_{D2} - i\omega)]$, thus a single Drude component with reweighted scattering cannot represent the two Drude components. In addition, the narrow Drude component only shows ordinary narrowing with decreasing temperature due to the metallic response and the evolution of this scattering rate is not related to the T^* phase transition. Therefore we just show the scattering rate $1/\tau_1$ of the broad Drude component in Fig. 5(b). The scattering rate $1/\tau_1$ is reduced by about 20% after the transition, indicating that the gap of the partial Fermi surface might reduce the scattering channels.

Although the electronic structure calculations give an estimation of loss of 30% of the electronic density of states across the T^* phase transition, there is no clue about the possible gap size at the Fermi surface supplied [16]. It is well known that the characteristic of a density-wave order transition is the formation of an energy gap near the Fermi level, which leads to a pronounced peak just above the energy gap in $\sigma_1(\omega)$ [25,30,31]. In this regard, the new peak formed below T^* ($\sim 3500\text{ cm}^{-1}$ at 10 K) could be identified as the CDW energy gap. However, the ratio of the energy gap relative to the transition temperature $2\Delta/k_B T_s$ reaches 33, which is

significantly higher than the BCS mean-field value of 3.5 for a density-wave phase transition [30]. This implies that the T^* phase transition temperature is much lower than the mean-field transition temperature. Usually, this phenomenon is attributed to a low-dimensional (e.g., 1D or 2D) electronic structure which gives rise to a strong fluctuation effect and suppresses the actual ordering temperature. Apparently, this scenario could not be applied here, since the $\text{Sr}_3\text{Ir}_4\text{Sn}_{13}$ compound is a 3D cubic material which is not supposed to cause strong fluctuation effects.

For correlated metals, the one-component approach is also often used in the analysis of infrared conductivity. In this approach the simple Drude model is extended by making the damping term in the Drude formula complex and frequency dependent [32]. This so-called extended Drude model has been extensively applied to transition-metal compounds, heavy-fermion systems, high- T_c cuprates, and other systems with electrons coupling strongly to certain bosonic excitations. Since the low-temperature specific heat analysis reveals a moderate enhancement of the electronic specific heat coefficient in $\text{Sr}_3\text{Ir}_4\text{Sn}_{13}$, we also conducted an extended Drude analysis of optical data and got the frequency-dependent scattering rate and the effective mass in terms of conductivity spectra [32],

$$\frac{1}{\tau(\omega)} = \frac{\omega_p^2}{4\pi} \frac{\sigma_1(\omega)}{\sigma_1^2(\omega) + \sigma_2^2(\omega)}, \quad (2)$$

$$\frac{m^*}{m_B} = \frac{\omega_p^2}{4\pi\omega} \frac{\sigma_2(\omega)}{\sigma_1^2(\omega) + \sigma_2^2(\omega)}, \quad (3)$$

where ω_p^2 is the unscreened overall plasma frequency, and m_B the band mass. The obtained spectra of the effective mass and the scattering rate with $\omega_p = 25\,750\text{ cm}^{-1}$ (at 10 K) are displayed in Fig. 6. Both the scattering rate and the effective mass show a pronounced temperature dependence at low frequencies. Notably, the scattering rate is suppressed below about 300 cm^{-1} , and correspondingly, the effective mass is strongly enhanced. This energy is about one order lower than the peak feature indicated in the above analysis. If this energy scale is related to the CDW energy gap, it would provide a natural explanation for the value of $2\Delta/k_B T_s$ predicted by the BCS theory. However, this is highly unlikely. In fact, the suppression feature is clearly present in the curves at 200 and 300 K, which is much higher than the phase transition temperature. From the conductivity spectra shown in Fig. 4(b) we clearly see the presence of two Drude components. The strong spectral change near 300 cm^{-1} in the effective mass and the scattering rate should be related to the two Drude components. On this basis, we believe that the Drude-Lorentz decomposition of $\sigma_1(\omega)$ is more appropriate here.

The surprisingly large value of the energy gap is a very puzzling phenomenon. It points towards an unconventional driving mechanism for the CDW phase transition in such material. It is worth noting that Varma and Simons proposed a strong-coupling theory of CDW transitions whose essential ingredients are the strong wave-vector dependence of electronically induced anharmonicity and mode-mode coupling [33]. This microscopic theory permits a value an order of magnitude larger than the BCS mean-field value of 3.5 and predicts that phonons over a substantial part of the Brillouin

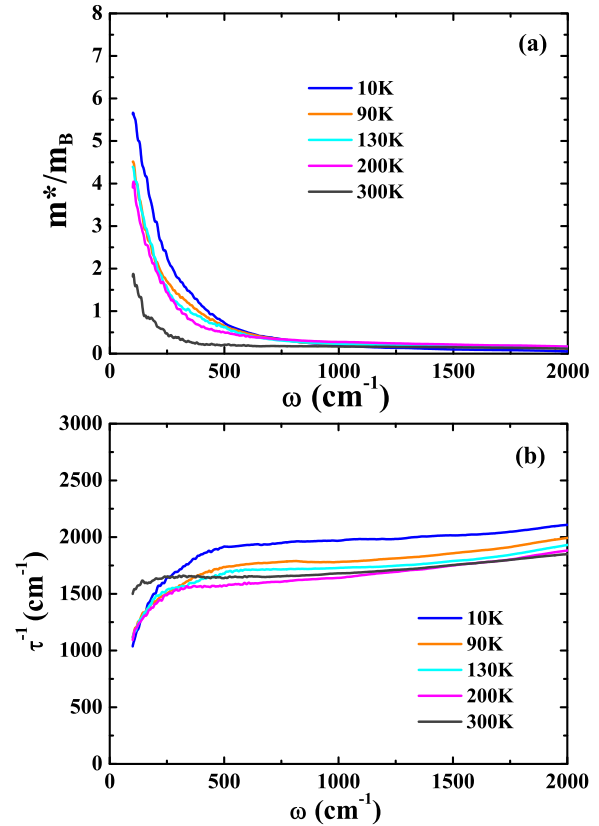


FIG. 6. (Color online) (a) Frequency dependence of the effective mass and (b) scattering rate of $\text{Sr}_3\text{Ir}_4\text{Sn}_{13}$.

zone are softened near the transition. The strong-coupling picture is also supported by the specific heat data. From the electronic specific heat coefficient $\gamma = 40\text{ mJ/K}^2\text{ mol}$ as derived from Fig. 3, we estimate the electronic heat capacity at the CDW transition temperature as roughly 6 J/K mol . The jump in the heat capacity at the transition shown in Fig. 2 is about $\Delta C \approx 60\text{--}70\text{ J/K mol}$. This leads to the ratio $\Delta C/C|_{T_{\text{CDW}}} \geq 10$, which is much higher than the value (1.43) of the simple mean-field BCS theory for CDW phase transition. In addition, according to the Fermi-liquid theory, γ is proportional to $n^{1/3}m^*$ ($\gamma = \frac{\pi^{2/3}k_B^2}{3^{2/3}\hbar^2} n^{1/3}m^*$) at low temperatures. In combination with the renormalized plasma frequency $(\omega_p^*)^2 = \frac{120}{\pi} \int_0^{\omega_c} \sigma_1(\omega)d\omega = \frac{4\pi n e^2}{m^*}$, we can obtain the values of the carrier density n and effective mass m^* [34,35]. Taking $\omega_c = 5000\text{ cm}^{-1}$, $n = 1.15 \times 10^{21}\text{ cm}^{-3}$ and $m^* = 4.53 m_e$ can be achieved. Therefore, due to the violation of weak-coupling BCS theory and the rather large effective mass, it is possible that $\text{Sr}_3\text{Ir}_4\text{Sn}_{13}$ is an example of such a strong-coupling CDW mechanism. Nevertheless, further studies are necessary on the unconventional CDW phase transition in such an intermetallic compound.

In summary, we have successfully grown single-crystal samples of $\text{Sr}_3\text{Ir}_4\text{Sn}_{13}$ and conducted careful characterizations by XRD, electrical resistivity, magnetic susceptibility, and specific heat measurements. The (110)-plane optical measurements of $\text{Sr}_3\text{Ir}_4\text{Sn}_{13}$ single crystals were performed to elucidate the nature of the T^* anomaly at 147 K. Bulk superconductivity is confirmed at 5 K. The optical spectroscopy reveals the

formation of a partial energy gap at the Fermi surface associated with the structural phase transition. It is estimated that the opening of the gap leads to the loss of 29% of itinerant carriers and a substantial reduction in the carrier scattering rate. An unconventional CDW scenario is suggested to explain the origin of the second-order phase transition. On the other hand, a spectral weight transfer is seen from the low-energy midinfrared region to the high-energy interband transition

region above 5000 cm^{-1} , both above and below the T^* phase transition, which is attributed to the electron correlation effect.

We thank C. M. Varma for helpful discussions. This work was supported by the National Science Foundation of China (Grant Nos. 11120101003 and 11327806) and the 973 project of the Ministry of Science and Technology of China (Grant Nos. 2011CB921701 and 2012CB821403).

-
- [1] J. A. Wilson, F. J. DiSalvo, and S. Mahajan, *Adv. Phys.* **24**, 117 (1975).
- [2] D. E. Moncton, J. D. Axe, and F. J. DiSalvo, *Phys. Rev. B* **16**, 801 (1977).
- [3] J. Dong, H. J. Zhang, G. Xu, Z. Li, G. Li, W. Z. Hu, D. Wu, G. F. Chen, X. Dai, J. L. Luo, Z. Fang, and N. L. Wang, *Europhys. Lett.* **83**, 27006 (2008).
- [4] C. de la Cruz, Q. Huang, J. W. Lynn, J. Y. Li, W. Ratcliff II, J. L. Zarestky, H. A. Mook, G. F. Chen, J. L. Luo, N. L. Wang, and P. C. Dai, *Nature* **453**, 899 (2008).
- [5] Y. Kamihara, T. Watanabe, M. Hirano, and H. Hosono, *J. Am. Chem. Soc.* **130**, 3296 (2008).
- [6] E. Morosan, H. W. Zandbergen, B. S. Dennis, J. W. G. Bos, Y. Onose, T. Klimczuk, A. P. Ramirez, N. P. Ong, and R. J. Cava, *Nature Phys.* **2**, 544 (2006).
- [7] J. J. Yang, Y. J. Choi, Y. S. Oh, A. Hogan, Y. Horibe, K. Kim, B. I. Min, and S.-W. Cheong, *Phys. Rev. Lett.* **108**, 116402 (2012).
- [8] A. F. Fang, T. Dong, H. P. Wang, Z. G. Chen, B. Cheng, Y. G. Shi, P. Zheng, G. Xu, L. Wang, J. Q. Li, and N. L. Wang, *Phys. Rev. B* **85**, 184520 (2012).
- [9] A. H. Castro Neto, *Phys. Rev. Lett.* **86**, 4382 (2001).
- [10] T. Valla, A. V. Fedorov, P. D. Johnson, P.-A. Glans, C. McGuinness, K. E. Smith, E. Y. Andrei, and H. Berger, *Phys. Rev. Lett.* **92**, 086401 (2004).
- [11] S. V. Borisenko, A. A. Kordyuk, V. B. Zabolotnyy, D. S. Inosov, D. Evtushinsky, B. Büchner, A. N. Yaresko, A. Varykhalov, R. Follath, W. Eberhardt, L. Patthey, and H. Berger, *Phys. Rev. Lett.* **102**, 166402 (2009).
- [12] S. Pyon, K. Kudo, and M. Nohara, *J. Phys. Soc. Jpn.* **81**, 053701 (2012).
- [13] A. F. Fang, G. Xu, T. Dong, P. Zheng, and N. L. Wang, *Sci. Rep.* **3**, 1153 (2013).
- [14] G. P. Espinosa, A. S. Cooper, and H. Barz, *Mater. Res. Bull.* **17**, 963 (1982).
- [15] N. Kase, H. Hayamizu, and J. Akimitsu, *Phys. Rev. B* **83**, 184509 (2011).
- [16] L. E. Klintberg, S. K. Goh, P. L. Alireza, P. J. Saines, D. A. Tompsett, P. W. Logg, J. Yang, B. Chen, K. Yoshimura, and F. M. Grosche, *Phys. Rev. Lett.* **109**, 237008 (2012).
- [17] S. Gerber, J. L. Gavilano, M. Medarde, V. Pomjakushin, C. Baines, E. Pomjakushina, K. Conder, and M. Kenzelmann, *Phys. Rev. B* **88**, 104505 (2013).
- [18] J. Yang, B. Chen, C. Michioka, and K. Yoshimura, *J. Phys. Soc. Jpn.* **79**, 113705 (2010).
- [19] G. P. Espinosa, *Mater. Res. Bull.* **15**, 791 (1980).
- [20] Z. G. Chen, G. Xu, W. Z. Hu, X. D. Zhang, P. Zheng, G. F. Chen, J. L. Luo, Z. Fang, and N. L. Wang, *Phys. Rev. B* **80**, 094506 (2009).
- [21] W. Z. Hu, G. Li, J. Yan, H. H. Wen, G. Wu, X. H. Chen, and N. L. Wang, *Phys. Rev. B* **76**, 045103 (2007).
- [22] T. Ishikawa, S. K. Park, T. Katsufuji, T. Arima, and Y. Tokura, *Phys. Rev. B* **58**, R13326(R) (1998).
- [23] T. Katsufuji, T. Tanabe, T. Ishikawa, Y. Fukuda, T. Arima, and Y. Tokura, *Phys. Rev. B* **54**, R14230(R) (1996).
- [24] Y. Okimoto, T. Katsufuji, T. Ishikawa, A. Urushibara, T. Arima, and Y. Tokura, *Phys. Rev. Lett.* **75**, 109 (1995).
- [25] M. Dressel and G. Grüner, *Electrodynamics of Solids: Optical Properties of Electrons in Matter* (Cambridge University Press, Cambridge, 2002).
- [26] D. A. Tompsett, *Phys. Rev. B* **89**, 075117 (2014).
- [27] D. J. Singh and M. H. Du, *Phys. Rev. Lett.* **100**, 237003 (2008).
- [28] D. Wu *et al.*, *Phys. Rev. B* **81**, 100512(R) (2010).
- [29] J. J. Tu, J. Li, W. Liu, A. Punnoose, Y. Gong, Y. H. Ren, L. J. Li, G. H. Cao, Z. A. Xu, and C. C. Homes, *Phys. Rev. B* **82**, 174509 (2010).
- [30] G. Grüner, *Density Waves in Solids* (Addison-Wesley, Reading, MA, 1994).
- [31] L. Degiorgi, M. Dressel, A. Schwartz, B. Alavi, and G. Grüner, *Phys. Rev. Lett.* **76**, 3838 (1996).
- [32] D. N. Basov and T. Timusk, *Rev. Mod. Phys.* **77**, 721 (2005).
- [33] C. M. Varma and A. L. Simons, *Phys. Rev. Lett.* **51**, 138 (1983).
- [34] L. Degiorgi, *Rev. Mod. Phys.* **71**, 687 (1999).
- [35] K. S. Burch, A. Schafgans, N. P. Butch, T. A. Sayles, M. B. Maple, B. C. Sales, D. Mandrus, and D. N. Basov, *Phys. Rev. Lett.* **95**, 046401 (2005).